

Constraints on local primordial non-Gaussianity from the large-scale clustering of DESI Luminous Red Galaxies

Mehdi Rezaie^{1,2}, Ashley J. Ross³, Hee-Jong Seo², Hui Kong³, Edmond Chaussidon⁴, Anna Porredon³, Lado Samushia¹, Rongpu Zhou⁵, Alex Krolewski^{6,7,8}, Arnaud de Mattia⁴, Jose Bermejo⁷, Florian Beutler⁹, Christophe Yèche⁴, Nathalie Palanque-Delabrouille^{4,5}, Klaus Honscheid^{3,10}, and DESI Members

¹*Department of Physics, Kansas State University, 116 Cardwell Hall, Manhattan, KS 66506, USA*

²*Department of Physics and Astronomy, Ohio University, Athens, OH 45701, USA*

³*Center for Cosmology and AstroParticle Physics, The Ohio State University, 191 West Woodruff Avenue, Columbus, OH 43210, USA*

⁴*IRFU, CEA, Université Paris-Saclay, F-91191 Gif-sur-Yvette, France*

⁵*Lawrence Berkeley National Laboratory, 1 Cyclotron Road, Berkeley, CA 94720, USA*

⁶*Department of Physics and Astronomy, University of Waterloo, 200 University Ave W, Waterloo, ON N2L 3G1, Canada*

⁷*Perimeter Institute for Theoretical Physics, 31 Caroline St. North, Waterloo, ON N2L 2Y5, Canada*

⁸*Waterloo Centre for Astrophysics, University of Waterloo, 200 University Ave W, Waterloo, ON N2L 3G1, Canada*

⁹*Institute for Astronomy, University of Edinburgh, Royal Observatory, Blackford Hill, Edinburgh EH9 3HJ, UK*

¹⁰*Department of Physics, The Ohio State University, 191 West Woodruff Avenue, Columbus, OH 43210, USA*

Accepted XXX. Received YYY; in original form ZZZ

ABSTRACT

This paper uses the large-scale clustering of luminous red galaxies selected from the Dark Energy Spectroscopic Instrument Legacy Imaging Surveys Data Release 9 to constrain the local primordial non-Gaussianity (PNG) parameter f_{NL} . Using the angular power spectrum, we thoroughly investigate the impact of various photometric systematic effects, such as those caused by Galactic extinction and varying survey depth. Simulations are utilized to construct covariance matrices, evaluate the robustness of our pipeline, and perform statistical tests to assess whether spurious fluctuations are properly mitigated and calibrated. Using modes from $\ell = 2$ to 300, we find $X1 < f_{\text{NL}} < X2$ with our conservative and $X1 < f_{\text{NL}} < X2$ with extreme treatment of imaging systematics, both at 68% confidence. While our results are consistent with zero PNG, but we show that the understanding of imaging systematics is of paramount importance to obtain unbiased constraints on f_{NL} .

Key words: cosmology: inflation - large-scale structure of the Universe

1 INTRODUCTION

Current observations of the cosmic microwave background, large-scale structure, and supernovae are explained by a cosmological model that consists of dark energy, dark matter, and ordinary luminous matter, which has gone through a phase of rapid expansion known as *inflation* (see, e.g., Weinberg et al. 2013). At the end of inflation, the universe was reheated and primordial fluctuations are created to seed the subsequent growth of structure. Statistical properties of primordial fluctuations still remain as one of the unsolved puzzles in modern observational cosmology. Analyses of cosmological data have revealed that initial conditions of the universe are consistent with Gaussian fluctuations; however, there are some classes of models that predict some levels of non-Gaussianities in the primordial gravitational field.

Primordial non-Gaussianity of the local type is parameterized by Komatsu & Spergel (2001),

$$\Phi = \phi + f_{\text{NL}}(\phi^2 - \langle \phi^2 \rangle), \quad (1)$$

where ϕ represents the primordial gravitational field and f_{NL} is the coefficient of the nonlinear correction to the primordial field. The most stringent constraints on f_{NL} comes from the three-point statistics of the CMB temperature anisotropies, $f_{\text{NL}} = 0.9 \pm 5.0$ (Akrami et al. 2019). However, it has been shown that PNG has a scale-dependent signature on the two-point clustering of biased tracers of dark matter gravitational field. The clustering of biased tracers is boosted on large scales by a scale-dependent shift proportional to k^{-2} (see, Dalal et al. 2008).

Previous studies of f_{NL} with galaxy and quasar clustering

have been hindered dramatically by spurious fluctuations in target density, which are due to the variation of imaging properties across the sky (Ho et al. 2015). For instance, Pullen & Hirata (2013) found that the level of systematic contamination in the quasar sample of SDSS DRX does not allow a robust f_{NL} measurement. These imaging systematic issues are expected to be severe for wide-area galaxy surveys that observe the night sky closer to the Galactic plane and select faint targets. Assuming imaging systematics are under control, the next generation of galaxy surveys such as DESI and the Rubin Observatory are forecast to yield unprecedented constraints on f_{NL} . Combined with CMB data, the limits can be enhanced to a precision level required to differentiate between single and multi-field inflationary models.

In this paper, we use photometric galaxies and quasars from the DESI Legacy Imaging Surveys Data Release 9 to constrain the primordial non-Gaussianity parameter f_{NL} , while marginalizing over bias and shotnoise parameters. We make use of spectroscopic data from DESI Survey Validation to determine the redshift distribution of galaxies. We cross correlate target density fields with the templates of imaging systematics to quantify systematic error and assess the effectiveness of systematics treatments and the significance of residual systematic error. The methodologies and statistical tools presented in this work will pave the path for future imaging surveys.

2 DATA

Luminous red galaxies are massive galaxies that lack active star formation and considered as one of the highly biased tracers of large scale structure. They are widely targeted in previous galaxy surveys CITE, and their clustering and redshift properties are well known CITE. We use the photometric DESI Luminous Red Galaxies (LRG), selected from the imaging surveys (Dey et al. 2018) using color-magnitude cuts described in the g , r , z , and $W1$ bands (see, Zhou et al. 2021), and summarized in Tab. 1. The LRG sample are masked for bright stars, foreground bright galaxies as well as clusters of galaxies¹, and then binned into HEALPix (Gorski et al. 2005) at $n_{\text{SIDE}} = 256$ to construct the LRG density field, with an average density of 800 deg^{-2} with a coverage around 14000 square degrees of the sky. Fig. 1 shows observed density field of DR9 LRGs in deg^{-2} . There are some disconnected islands, hereafter referred to as *spurious islands*, in the DECaLS North region at Declination below -11 , which are removed from the sample to minimize potential calibration issues. Additionally, parts of the DECaLS South with Declination below -30 are cut from the sample, since similar calibration issues might infect our analysis. Section 4 presents how these cuts might alter constraints. DESI imaging is a multi-epoch dataset, and thus LRG density map is accounted for pixel incompleteness using a catalog of random points, uniformly scattered over the footprint with the same cuts and masks as DR9 LRGs. Fig. 2 shows the redshift distribution of DR9 LRGs inferred from DESI Survey Validation CITE and the evolution of galaxy bias for our LRG sample adapted from Zhou et al. (2021), consistent with the assumption of constant clustering amplitude.

We study the correlation coefficient between the LRG density map and potential sources of systematic error, mapped into HEALPix at the same n_{SIDE} . The maps used in this work are local stellar density constructed from point-like sources with a g -band

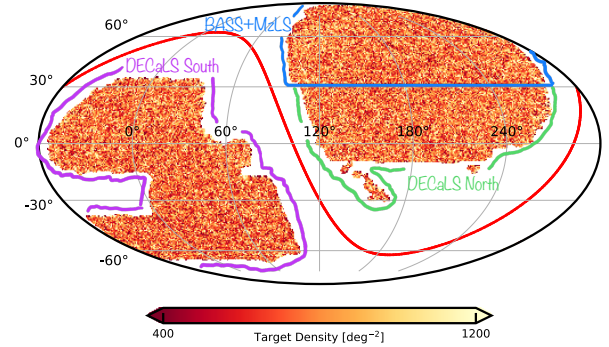


Figure 1. Observed density field of DESI Luminous Red Galaxies Data Release 9 in deg^{-2} . Spurious islands from the DECaLS North footprint at Declination below -11 and parts of the DECaLS South with Declination below -30 are dropped from the DR9 sample due to potential calibration issues.

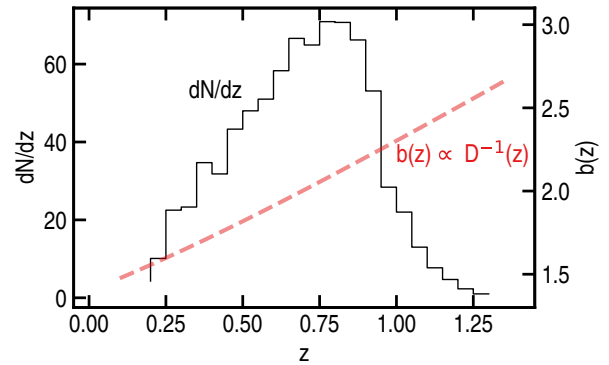


Figure 2. Redshift distribution and bias evolution of DESI LRGs with the assumption of constant clustering amplitude.

magnitude in the range $12 \leq g < 17$ from Gaia Data Release 2 (see, Gaia Collaboration et al. 2018; Myers et al. 2022), Galactic extinction $E[B-V]$ from Schlegel et al. (1998), and other imaging properties including survey depth (galaxy depth in grz and PSF depth in $W1$) and seeing in grz from DESI imaging. Fig. 4 shows the Spearman correlation between galaxy density and imaging properties.

3 METHODOLOGY

3.1 Measuring Power Spectrum

Galaxy density contrast in pixel i is defined as,

$$\hat{\delta}_i = \frac{\rho_i}{\hat{\rho}} - 1, \quad (2)$$

where ρ is the density of galaxies accounted for pixel area $f_{\text{pix},i}$ and $\hat{\rho}$ is the mean galaxy density estimated by,

$$\hat{\rho} = \frac{\sum_i \rho_i f_{\text{pix},i}}{\sum_i f_{\text{pix},i}}. \quad (3)$$

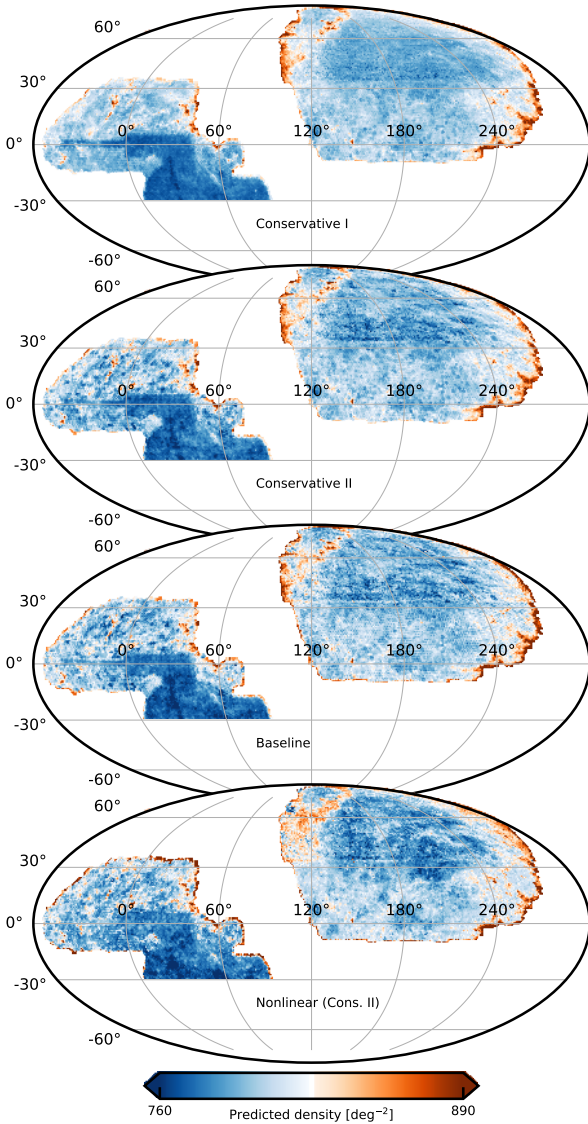
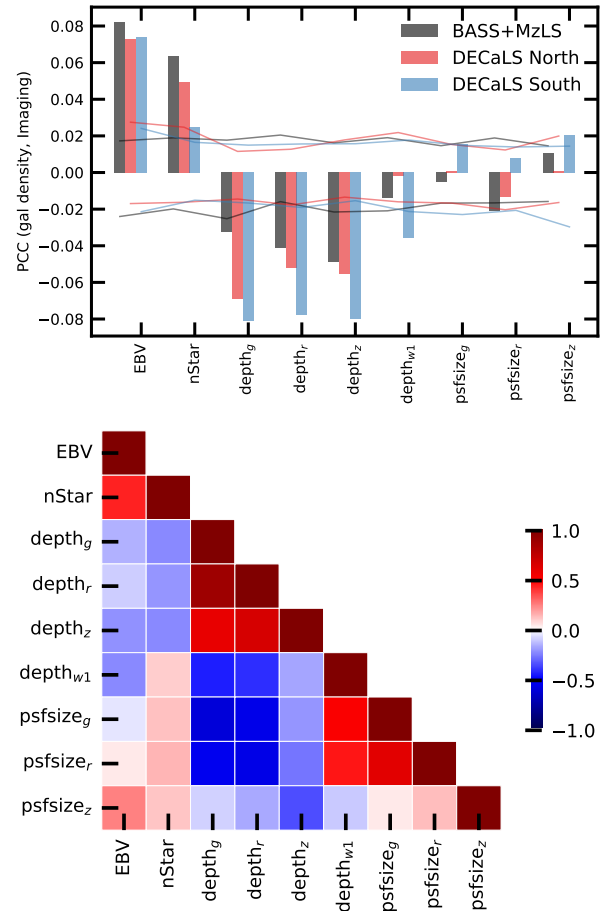
By definition, Eqs. 2 and 3 ensure that the integral of the observed quantity over the footprint vanishes:

$$\sum_i \hat{\delta}_i f_{\text{pix},i} = 0, \quad (4)$$

¹ See <https://www.legacysurvey.org/dr9/bitmasks/>

Table 1. Selection criteria for the LRG targets.

Criterion	Description
DECaLS	
$z_{\text{fiber}} < 21.7$	faint limit
$z - W1 > 0.8 \times (r - z) - 0.6$	Stellar rejection
$[(g - r > 1.3) \text{ AND } ((g - r) > -1.55 * (r - W1) + 3.13)] \text{ OR } (r - W1 > 1.8)$	Remove low-z galaxies
$[(r - W1 > (W1 - 17.26) * 1.8) \text{ AND } (r - W1 > W1 - 16.36)] \text{ OR } (r - W1 > 3.29)$	Luminosity cut
BASS+MzLS	
$z_{\text{fiber}} < 21.71$	faint limit
$z - W1 > 0.8 \times (r - z) - 0.6$	Stellar rejection
$[(g - r > 1.34) \text{ AND } ((g - r) > -1.55 * (r - W1) + 3.23)] \text{ OR } (r - W1 > 1.8)$	Remove low-z galaxies
$[(r - W1 > (W1 - 17.24) * 1.83) \text{ AND } (r - W1 > W1 - 16.33)] \text{ OR } (r - W1 > 3.39)$	Luminosity cut


Figure 3. Predicted galaxy counts from template regression. Baseline approach uses imaging maps from Zhou et al. (2022): EBV, galaxy depth in rgz, psfdepth in W1, and psfsize in grz. Conservative I uses EBV and galaxy depth in z, and Conservative II uses EBV, galaxy depth in z, and psfsize in r. In all approaches, the models are regressed on BASS+MzLS, DECaLS North, and DECaLS South separately.

Figure 4. Top: Pearson-r correlation coefficient between galaxy density and imaging properties in the three imaging regions (top) and between imaging properties themselves for the full DESI footprint (bottom). Solid curves represent the range of correlations observed in 100 randomly selected mock realizations.

To estimate power spectrum, we expand the galaxy overdensity field in terms of Legendre polynomials,

$$\delta_i = \sum_{\ell=0}^{\ell_{\max}} \sum_{m=-\ell}^{\ell} a_{\ell m} Y_{\ell m}(\theta_i, \phi_i), \quad (5)$$

where θ, ϕ represent the polar and azimuthal angular coordinates of pixel i , respectively. The cutoff at $\ell = \ell_{\max}$ assumes that modes

with $\ell > \ell_{\max}$ do not contribute significantly to signal power. The coefficients $a_{\ell m}$ are then obtained by integrating the density contrast field over the total number of non-empty pixels N_{pix} and using the orthogonality of Legendre polynomials:

$$\hat{a}_{\ell m} = \frac{4\pi}{N_{\text{pix}}} \sum_{i=1}^{N_{\text{pix}}} \delta_i f_{\text{pix},i} Y_{\ell m}^*(\theta_i, \phi_i), \quad (6)$$

where $*$ represents the complex conjugate. Then, the angular power spectrum estimator is defined as the variance of $\hat{a}_{\ell m}$ coefficients:

$$\hat{C}_\ell = \frac{1}{2\ell+1} \sum_{m=-\ell}^{\ell} \hat{a}_{\ell m} \hat{a}_{\ell m}^*. \quad (7)$$

In order to extract $\hat{a}_{\ell m}$ and compute the angular power spectrum, C_ℓ , we make use of the ANAFast function from HEALPix (Gorski et al. 2005) with the third order iteration of the quadrature to increase the accuracy². Due to the survey geometry implicit in the summation over the non-empty pixels and explicit in $f_{\text{pix},i}$, our estimator does not return an unbiased estimate of power spectrum, and thus the same effect must be accounted in the modeling of power spectrum. We ignore $\ell = 0$ and 2 and bin spectra with $\Delta\ell = 10$ up to $\ell_{\max} =$

3.2 Modeling Power Spectrum

The projected angular power spectrum of galaxies in the presence of redshift space distortions and local primordial non-Gaussianity is related to the 3D linear power spectrum $P(k)$ and shotnoise N_{shot} by (see, e.g., Slosar et al. 2008),

$$C_\ell = \frac{2}{\pi} \int_0^\infty \frac{dk}{k} k^3 P(k) |\Delta_\ell(k)|^2 + N_{\text{shot}}, \quad (8)$$

where $\Delta_\ell(k) = \Delta_\ell^g(k) + \Delta_\ell^{\text{RSD}}(k) + \Delta_\ell^{\text{fNL}}(k)$ and,

$$\Delta_\ell^g(k) = \int \frac{dr}{r} r b(r) D(r) \frac{dN}{dr} j_\ell(kr), \quad (9)$$

$$\Delta_\ell^{\text{RSD}}(k) = - \int \frac{dr}{r} r f(r) D(r) \frac{dN}{dr} j_\ell''(kr), \quad (10)$$

$$\Delta_\ell^{\text{fNL}}(k) = f_{\text{NL}} \frac{\alpha}{k^2 T(k)} \int \frac{dr}{r} r [b(r) - p] \frac{dN}{dr} j_\ell(kr), \quad (11)$$

where $\alpha = 3\delta_c \Omega_M (H_0/c)^2$, $b(r)$ is the linear bias, dN/dr is the normalized redshift distribution of galaxies³, $D(r)$ is the normalized growth factor such that $D(0) = 1$, $f(r)$ is the growth rate, and r is the comoving distance. The parameter p is the response of the tracer to halo's gravitational field, e.g., 1 for luminous red galaxies and 1.6 for recent mergers. In order to overcome rapid oscillations in spherical Bessel functions, we employ the FFTLog⁴ algorithm and its extension as implemented in ? to compute the inner integrations over $d \ln r$.

3.2.1 Survey Geometry

For a galaxy survey that observes the sky partially, the measured power spectrum is convolved with the survey geometry. This means

that the pseudo-power spectrum \hat{C}_ℓ obtained by the direct Spherical Harmonic Transforms of a partial sky map, differs from the full-sky angular spectrum C_ℓ . However, their ensemble average is related by (?)

$$\langle \hat{C}_\ell \rangle = \sum_{\ell'} M_{\ell\ell'} \langle C_{\ell'} \rangle, \quad (12)$$

where $M_{\ell\ell'}$ represents the mode-mode coupling from the partial sky coverage. This is known as the Window Function effect and a proper assessment of this effect is crucial for a robust measurement of the large-scale clustering of galaxies. This window effect is a source of observational systematic error and impacts the measured galaxy clustering, especially on scales comparable to survey size.

We follow a similar approach to that of (?) to model the window function effect on the theoretical power spectrum C_ℓ rather than correcting the measured pseudo-power spectrum from data. First, we use HEALPIX to compute the pseudo-power spectrum of the window $\hat{C}_\ell^{\text{window}}$, which is defined by a mask file in ring ordering format with NSIDE= 256. Then, we transform it to correlation function by,

$$\omega^{\text{window}}(\theta) = \frac{1}{4\pi} \sum_{\ell} (2\ell+1) \hat{C}_\ell^{\text{window}} P_\ell(\cos \theta). \quad (13)$$

Next, we normalize ω^{window} such that it is normalized to one at $\theta = 0$. Finally, we multiply the theory correlation function by ω^{window} and transform the result back to ℓ -space,

$$\hat{\omega}^{\text{model}} = \omega^{\text{model}} \omega^{\text{window}} \quad (14)$$

$$\hat{C}_\ell^{\text{model}} = 2\pi \int d\theta \hat{\omega}^{\text{model}}(\theta) P_\ell(\cos \theta). \quad (15)$$

3.2.2 Integral Constraint

The integral of the galaxy density contrast δ on the footprint is bound to zero, which is often referred to as the *Integral Constraint*. We account for this effect in the modeling by,

$$\hat{C}_\ell^{\text{model,IC}} = \hat{C}_\ell^{\text{model}} - \hat{C}_{\ell=0}^{\text{model}} \left(\frac{\hat{C}_\ell^{\text{window}}}{\hat{C}_{\ell=0}^{\text{window}}} \right) \quad (16)$$

3.3 Characterization of systematic effects

We use the diagnostic tests presented in Rezaie et al 2021 based on cross power spectrum between galaxy density field and imaging maps and mean density contrast as a function of imaging properties to quantify the significance of imaging systematic effects.

3.3.1 Cross Spectrum

Taking $C_\ell^{g,x}$ as the cross power spectrum between galaxy density contrast field and imaging map, one can normalize this quantity by auto power spectrum of imaging map itself:

$$\hat{C}_{x,\ell} = \frac{(\hat{C}_\ell^{g,x})^2}{\hat{C}_\ell^{x,x}}, \quad (17)$$

and then construct a vector from cross spectra against all other imaging maps:

$$\hat{C}_{X,\ell} = [\hat{C}_{x_1,\ell}, \hat{C}_{x_2,\ell}, \hat{C}_{x_3,\ell}, \dots, \hat{C}_{x_9,\ell}]. \quad (18)$$

² We refer the reader to <https://healpix.sourceforge.io/pdf/subroutines.pdf>, p. 104-105.

³ $dN/dr = (dN/dz) * (dz/dr) \propto (dN/dz) * H(z)$

⁴ github.com/xfangcosmo/FFTLog-and-beyond

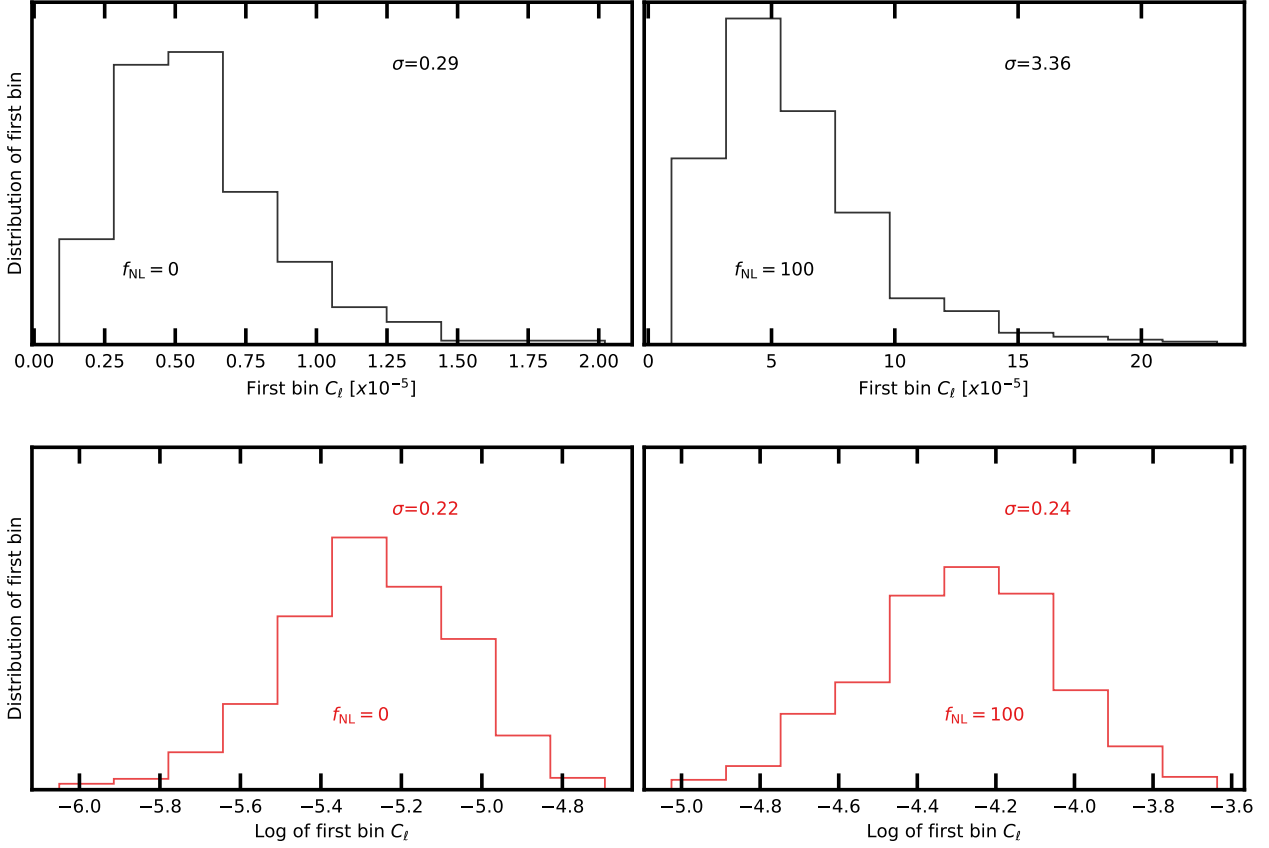


Figure 5. Distribution of the first bin power spectrum for $f_{\text{NL}} = 0$ and 100 mocks.

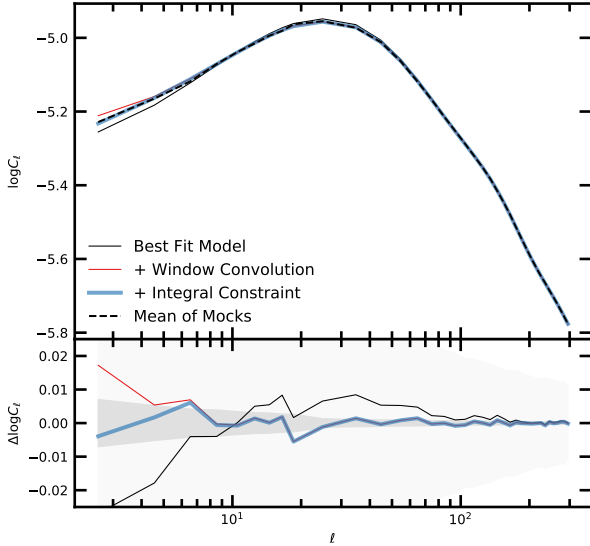


Figure 6. Mean power spectrum of 1000 mocks with $f_{\text{NL}} = 0$ and best fit theoretical prediction after accounting for various theoretical systematic effects.

We bin the C_X measurements with ℓ edges defined at 2, 10, 18, 26, 40, 60, 80, and 100. The mean and standard deviation of $\hat{C}_{X,\ell}$ for 1000 mocks with and without f_{NL} are shown in

Fig. 7. Finally, cross power spectrum χ^2 can be defined as,

$$\chi^2 = C_{X,\ell}^T C^{-1} C_{X,\ell}, \quad (19)$$

where covariance matrix $C = \langle C_{X,\ell} C_{X,\ell'} \rangle$ is constructed from mocks without systematic effects. This statistics is measured for every mock realization with the leave-one-out technique to construct a histogram, which is then compared to the χ^2 value observed from the DR9.

3.3.2 Mean Density

As an alternative test, we calculate the histogram of the density contrast field relative to each imaging map.

$$\delta_x = (\hat{\rho})^{-1} \frac{\sum_i \rho_i f_{\text{pix},i}}{\sum_i f_{\text{pix},i}}, \quad (20)$$

where the summations are over pixels in each bin of imaging map x . Similarly, we construct the mean density contrast vector against all imaging maps,

$$\delta_X = [\delta_{x_1}, \delta_{x_2}, \delta_{x_3}, \dots, \delta_{x_9}], \quad (21)$$

and the total residual error as,

$$\chi^2 = \delta_X^T C^{-1} \delta_X, \quad (22)$$

where the covariance matrix $C = \langle \delta_X \delta_X \rangle$ is constructed from mocks without systematic effects. Fig. 7 shows the cross power spectrum and mean density contrast for the DR9 LRG sample. The shades represent the 1σ level fluctuations observed in 1000 clean mocks with $f_{\text{NL}} = 0$ and 100.

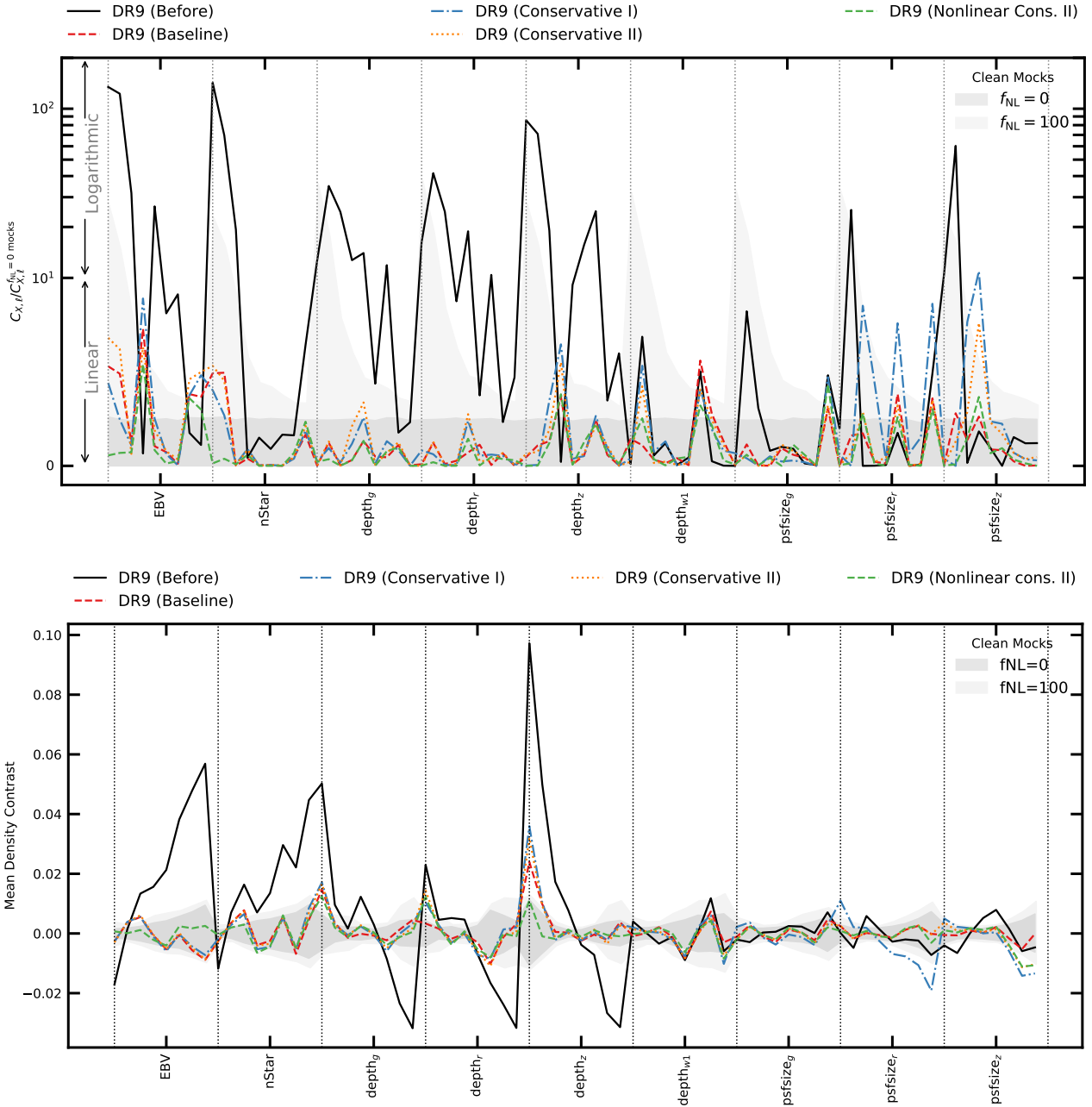


Figure 7. Residual systematic fluctuations of DR9 LRGs against imaging maps. Left: cross spectrum. Right: mean density contrast. Shades represent 1σ dispersion of 1000 clean mocks with and without f_{NL} .

4 RESULTS

4.1 Lognormal Mocks

Corner plots of the PNG parameter f_{NL} and bias coefficient are shown in Fig. 9 for fitting the mean power spectrum of the mocks, with and without f_{NL} . Maximum-A-Posteriori estimates and marginalized mean, median and 1σ quantiles are summarized in Tab. 2. Comparing DECaLS North with sky coverage 0.14 to full DESI with 0.40, we find the constraint improve by a factor of 1.9 which is slightly more than $\sim f_{\text{SKY}}^{-1/2}$, 1.7. while As a robustness test, we also fit the mean power spectrum of the $f_{\text{NL}} = 100$ mocks using the covariance matrix estimated from the $f_{\text{NL}} = 0$ mocks. We

find that the constraints improve by a factor of 4.2, due to a higher signal to noise ratio.

4.2 DR9 LRGs

5 CONCLUSION

ACKNOWLEDGEMENTS

DATA AVAILABILITY

REFERENCES

Akrami Y., et al., 2019, arXiv preprint arXiv:1905.05697

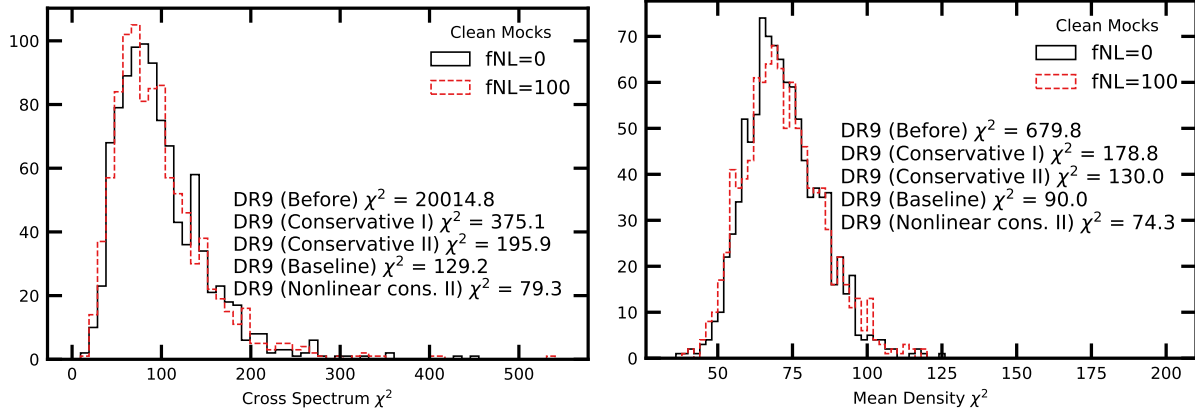


Figure 8. Left: Cross power spectrum χ^2 diagnostic. Right: Mean density contrast diagnostic. The values observed in DR9 before and after linear and nonlinear treatments are quoted and the histograms are constructed from 1000 realizations of clean mocks with $f_{\text{NL}} = 0$ and 100.

Table 2. Maximum-A-Posteriori (MAP) and marginalized mean estimates for f_{NL} from fitting the mean power spectrum of the mocks.

Mock f_{NL} / Footprint	Observable	Best fit	Mean	68% CL	95% CL
$f_{\text{NL}} = 100$ / DESI	$\log C_\ell$	100.97	100.97	$100.33 < f_{\text{NL}} < 101.61$	$99.72 < f_{\text{NL}} < 102.23$
	$\log C_\ell$ using $f_{\text{NL}} = 0$ cov	101.01	101.03	$100.42 < f_{\text{NL}} < 101.63$	$99.85 < f_{\text{NL}} < 102.21$
	C_ℓ	100.97	100.95	$100.32 < f_{\text{NL}} < 101.58$	$99.71 < f_{\text{NL}} < 102.18$
	C_ℓ using $f_{\text{NL}} = 0$ cov	100.13	100.13	$100.00 < f_{\text{NL}} < 100.26$	$99.88 < f_{\text{NL}} < 100.38$
$f_{\text{NL}} = 0$ / DESI	$\log C_\ell$	0.47	0.47	$0.08 < f_{\text{NL}} < 0.85$	$-0.30 < f_{\text{NL}} < 1.22$
DECaLS North		0.09	0.08	$-0.61 < f_{\text{NL}} < 0.78$	$-1.29 < f_{\text{NL}} < 1.45$
DECaLS South		0.87	0.88	$0.16 < f_{\text{NL}} < 1.58$	$-0.52 < f_{\text{NL}} < 2.27$
BASS+MzLS		1.07	1.07	$0.32 < f_{\text{NL}} < 1.82$	$-0.40 < f_{\text{NL}} < 2.55$

Table 3. Maximum-A-Posteriori (MAP) and marginalized mean estimates for f_{NL} from fitting power spectrum of DR9 LRGs for DESI footprint before and after correcting for systematics.

Footprint	Method	Best fit	Mean	68% CL	95% CL
DESI	No Weight	147.13	150.13	$127.58 < f_{\text{NL}} < 172.76$	$108.56 < f_{\text{NL}} < 197.07$
DESI	Baseline	46.87	49.04	$33.97 < f_{\text{NL}} < 63.98$	$21.21 < f_{\text{NL}} < 81.00$
	Conservative I	64.46	66.69	$49.67 < f_{\text{NL}} < 83.63$	$35.64 < f_{\text{NL}} < 102.59$
	Conservative II	47.62	49.54	$34.21 < f_{\text{NL}} < 64.81$	$21.27 < f_{\text{NL}} < 82.06$
	Nonlinear (Cons. II)	37.15	38.73	$24.58 < f_{\text{NL}} < 52.77$	$12.32 < f_{\text{NL}} < 68.55$
BASS+MzLS	Nonlinear (Cons. II)	20.06	24.71	$-1.52 < f_{\text{NL}} < 51.26$	$-24.95 < f_{\text{NL}} < 82.62$
DECaLS North		53.33	58.36	$30.33 < f_{\text{NL}} < 86.81$	$6.45 < f_{\text{NL}} < 120.93$
DECaLS South		40.61	43.17	$19.36 < f_{\text{NL}} < 68.11$	$-6.64 < f_{\text{NL}} < 96.65$
DECaLS North [incl. DEC < -11]		53.36	58.27	$30.65 < f_{\text{NL}} < 85.91$	$8.33 < f_{\text{NL}} < 118.84$
DECaLS South [incl. DEC < -30]		56.93	60.83	$39.20 < f_{\text{NL}} < 82.44$	$21.30 < f_{\text{NL}} < 107.53$

Dalal N., Dore O., Huterer D., Shirokov A., 2008, *Physical Review D*, 77, 123514
Dey A., et al., 2018, arXiv preprint arXiv:1804.08657
Gaia Collaboration et al., 2018, *A&A*, 616, A1
Gorski K. M., Hivon E., Banday A. J., Wandelt B. D., Hansen F. K., Reinecke M., Bartelmann M., 2005, *The Astrophysical Journal*, 622, 759
Ho S., et al., 2015, *J. Cosmology Astropart. Phys.*, 2015, 040
Komatsu E., Spergel D. N., 2001, *Physical Review D*, 63, 063002
Myers A. D., et al., 2022, arXiv e-prints, p. arXiv:2208.08518
Pullen A. R., Hirata C. M., 2013, *Publications of the Astronomical Society of the Pacific*, 125, 705
Schlegel D. J., Finkbeiner D. P., Davis M., 1998, *The Astrophysical Journal*, 500, 525

Slosar A., Hirata C., Seljak U., Ho S., Padmanabhan N., 2008, *Journal of Cosmology and Astroparticle Physics*, 2008, 031
Weinberg D. H., Mortonson M. J., Eisenstein D. J., Hirata C., Riess A. G., Rozo E., 2013, *Physics reports*, 530, 87
Zhou R., et al., 2021, *Monthly Notices of the Royal Astronomical Society*, 501, 3309

This paper has been typeset from a \LaTeX file prepared by the author.

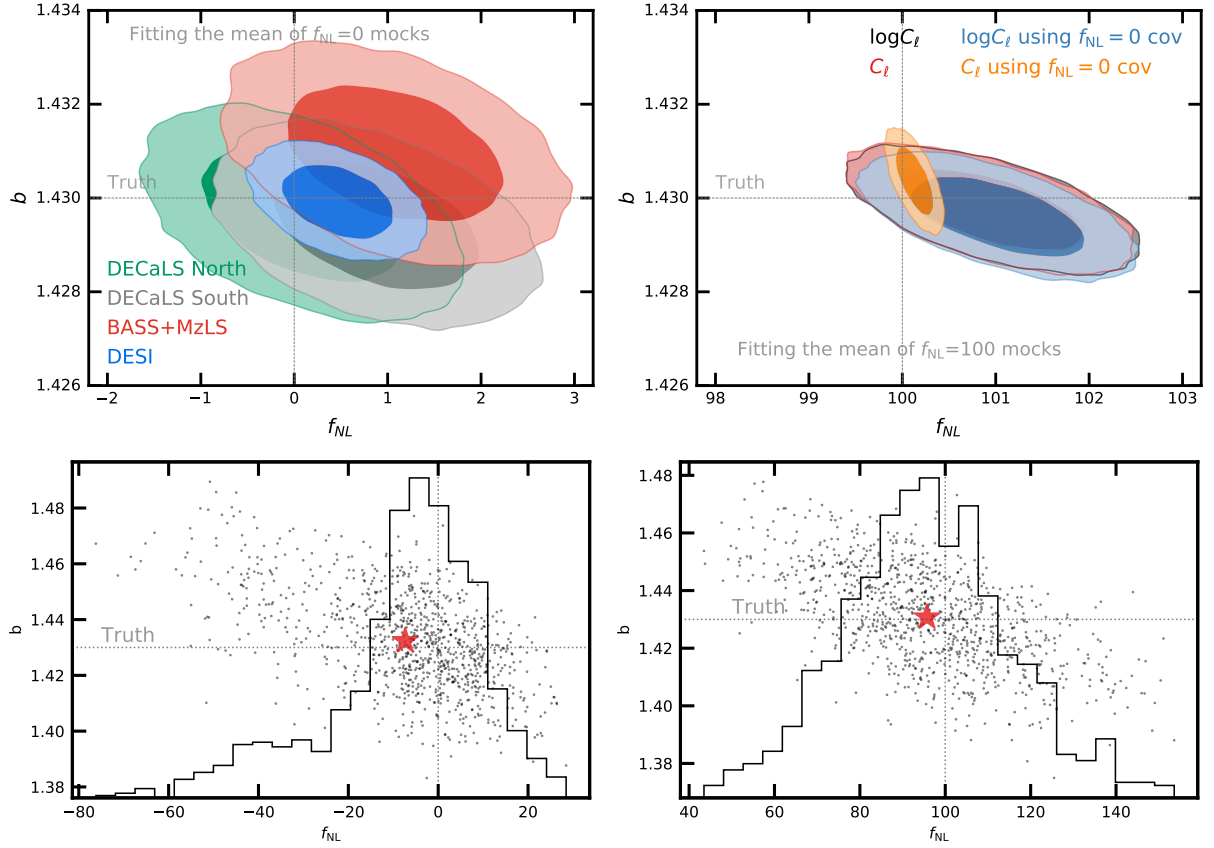


Figure 9. 68% and 95% confidence contours for $f_{\text{NL}} = 0$ and 100 mocks. bottom: best fit estimates.

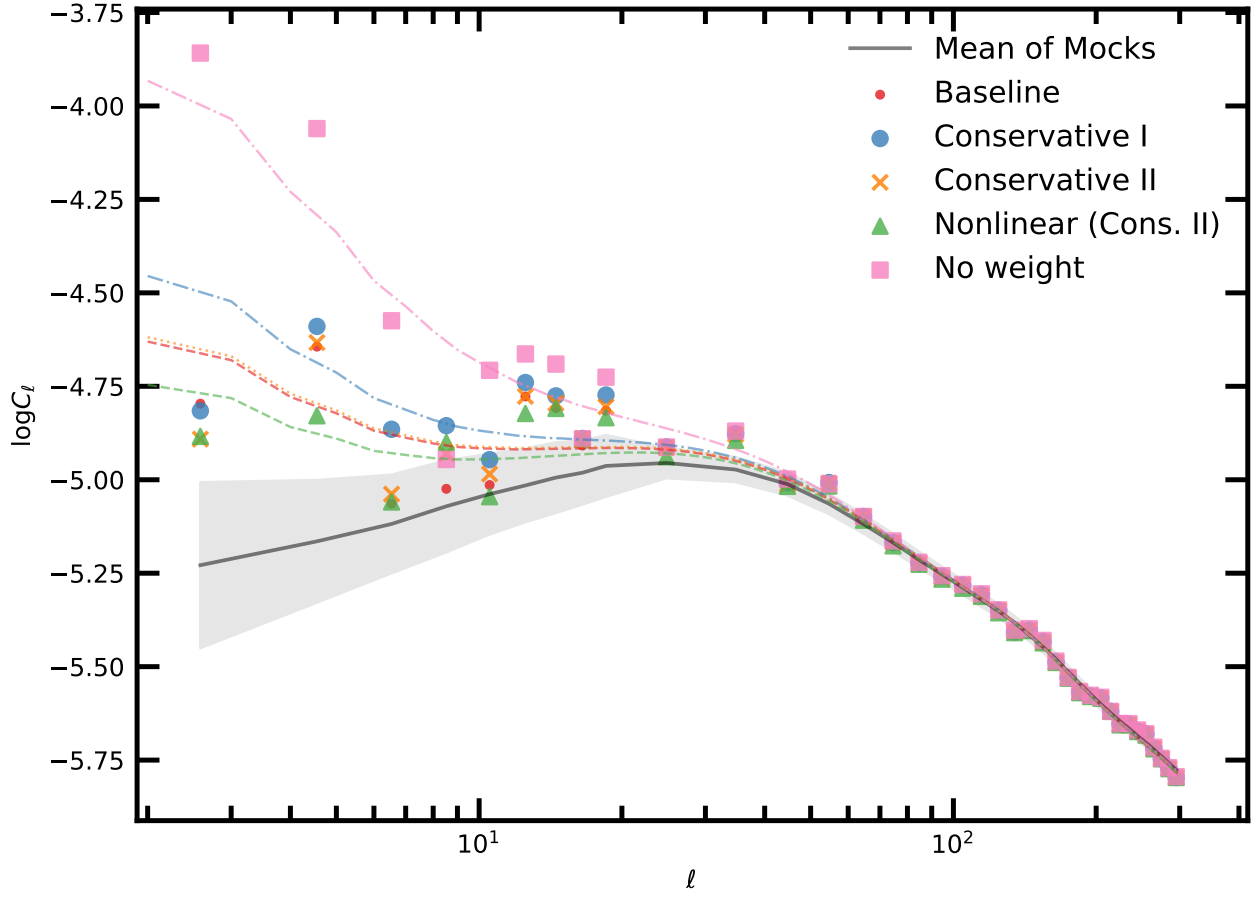


Figure 10. Measured power spectrum of the DR9 LRG sample before and after correcting for systematics with their corresponding best fit theory predictions. The shade represents 1σ error on the mean power spectrum of mocks.

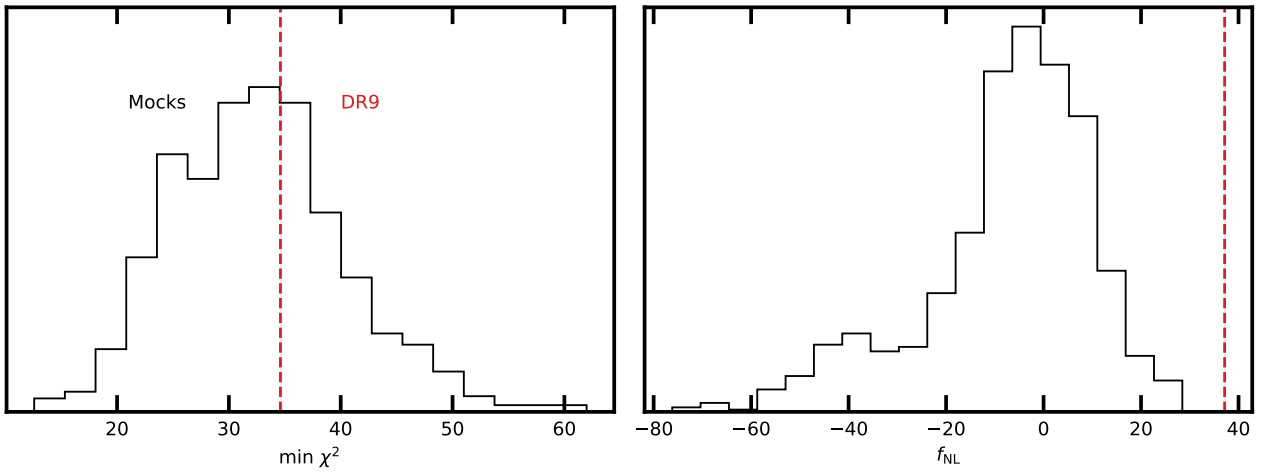
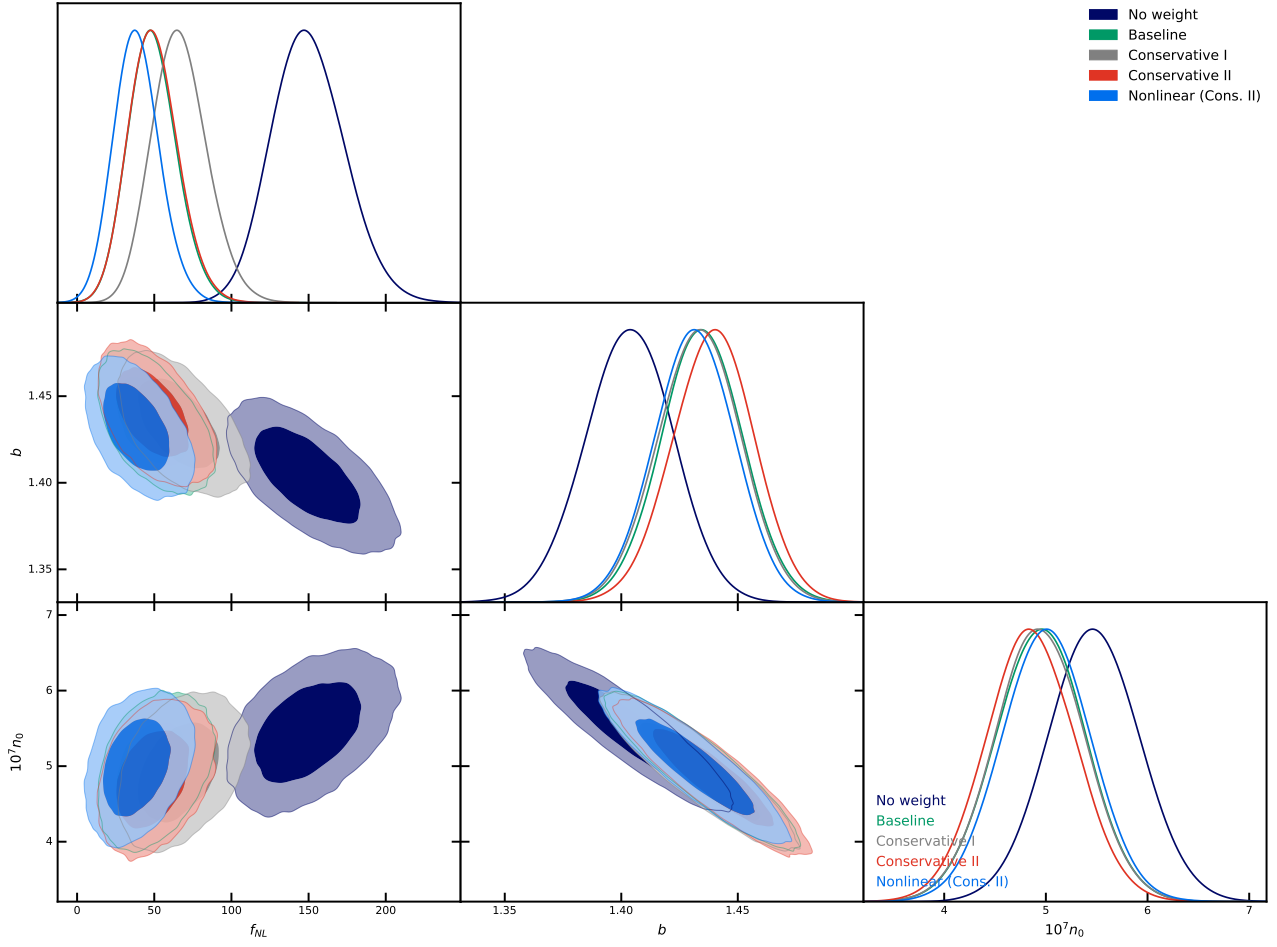


Figure 11.

**Figure 12.** DR9 LRGs for DESI footprint.

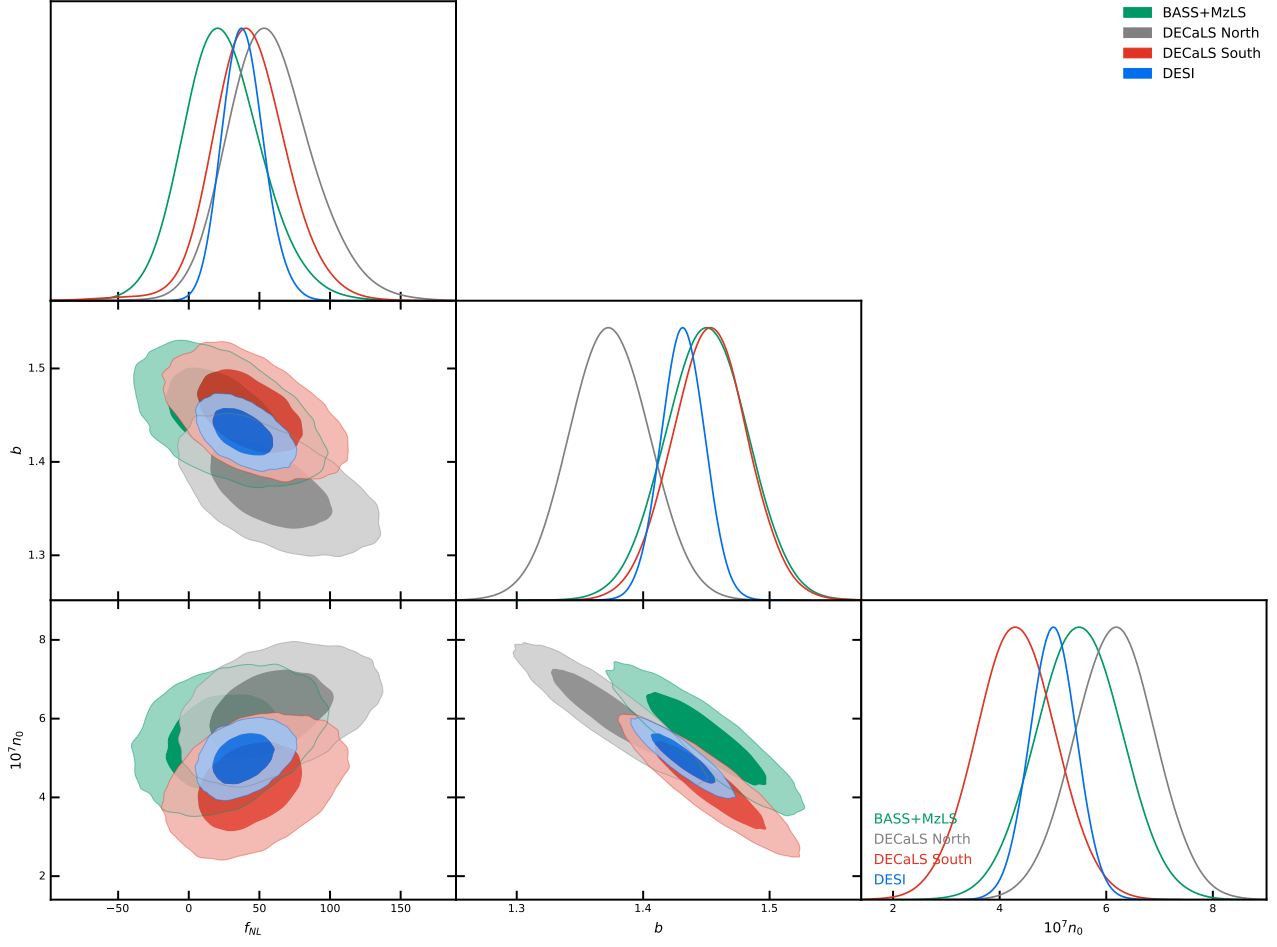


Figure 13. DR9 LRGs for each individual imaging survey.

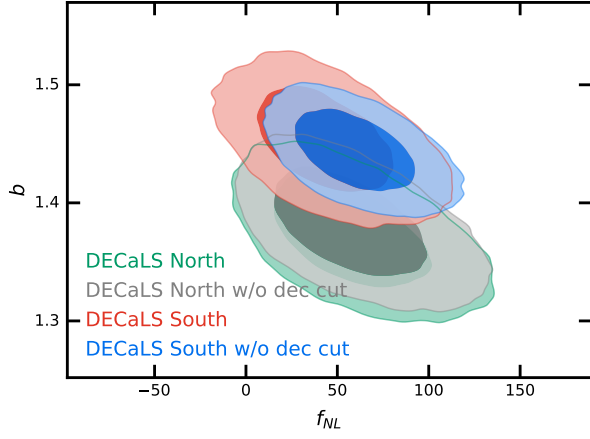


Figure 14. Impact of cutting out spurious islands in DECaLS North and DEC < -30 in DECaLS South.